Highly active hydrogen evolution catalysis on oxygen-deficient double-perovskite oxide PrBaCo_2O_6−δ

ARTICLE

Highly active hydrogen evolution catalysis on oxygen-deficient double-perovskite oxide PrBaCo$_2$O$_{6-\delta}$

Hayato Togano,[a] Kaisei Asai,[a] Seiji Oda,[a] Hidekazu Ikeno,[a] Shogo Kawaguchi,[b] Kengo Oka,[c] Kouhei Wada,[d] Shunsuke Yagi[e] and Ikuya Yamada*[a]

Efficient hydrogen evolution on water splitting is a crucial issue to achieve a sustainable society based on renewable energy. Highly active and cost-effective catalysts for oxygen/hydrogen evolution reactions (OER/HERs) are desired to suppress their intrinsically significant overpotentials. Perovskite-related transition-metal oxides have been widely investigated as promising candidates for electrochemical catalysts, whereas complex compositions and structures inhibit elucidation of essential factors to activate HER. Herein, we report a systematic study on predominant factors affecting HER catalysis for Co-containing perovskite-related oxides. The A-site-ordered double perovskite oxide PrBaCo$_2$O$_{6-\delta}$ exhibits HER activity with a volcano-type plot associated with oxygen deficiency content, and leads to the highest activity at a moderate value of δ = 0.2, in addition to the significant superiority to the simple ABO$_3$-type perovskite, ACoO$_3$ (A = La, La$_{0.5}$Ca$_{0.5}$, Ca). Based on Tafel slope, electric conductivity, and charge-transfer resistance analyses, we have found that complementary factors dominate the HER catalysis; Co–O covalency and water dissociation site, which are respectively induced by high Co valence and oxygen deficiency. This finding provides new insight into the rational design of transition-metal oxide catalysts for HER.

1. Introduction

Water splitting by using renewable energy sources is considered as one of the most promising ways to achieve clean hydrogen generation system.[1–3] Kinetic limitations for anodic/cathodic reactions of oxygen/hydrogen evolution reactions (OER/HERs) cause large overpotentials to decrease energy conversion efficiency. Precious-metal-based catalysts, (Ru/Ir)O$_2$ and Pt, have been widely utilized as the most efficient catalysts for OER and HER, respectively.[4] However, further developments of catalysts consisting of cost-effective and earth-abundant elements are desired for large-scale applications.

Perovskite-related transition metal oxides have been extensively investigated as promising candidates for OER catalysts. After systematic studies on simple ABO$_3$-type perovskite oxides three decades ago,[5,6] several mixed-metal perovskite oxides were recently proposed as highly active OER catalysts.[7–15] Rational descriptors such as e$_g$ electron occupancy,[7] oxygen 2p band center,[8] and charge-transfer energy[16–19] were

also proposed to design OER catalysts. In contrast, HER catalysis on perovskite oxides have not been well investigated due to their poor conversion from hydrogen intermediates to H$_2$.[20,21] Recent advances on perovskite-related HER catalysts[22–27] arouse further exploration for highly active HER catalysts based on rational design principle. The A-site-ordered double perovskite oxides, RBaCo$_2$O$_{6-\delta}$ (R: rare-earth metal), have been commonly investigated for OER catalysts. Grimaud et al. proposed these compounds as a member of highly active OER catalysts, in which OER activity systematically changes by R ions.[8] The varied OER activity for this system was interpreted by using oxygen 2p band center energy as a descriptor. Recently, potential of the double perovskite oxides as HER catalysts has also been examined. Guan et al. demonstrated that oxygen deficiency sites in RBaCo$_2$O$_{6-\delta}$ facilitates H$_2$O adsorption, whereas lowered electric conductivity and Co valence are unfavorable for HER.[25] In addition, it has been recently proposed that the HER activity is dominated by A-site ionic electronegativity.[26] Since the proposed factors were based on the examination of various kinds of compounds, a systematic study on the simple compound is needed to provide deep insight into the relationship between HER activity and the aforementioned factors. PrBaCo$_2$O$_{6-\delta}$ (PBCO$_{6-\delta}$) crystallizes in double perovskite structure with layered-type A-site ordering (see the crystal structure in Figure 1 drawn by using VESTA-3 program[28]). A wide range of oxygen deficiency content and resulting Co valence states are achievable in this system by using various synthesis conditions including high pressure,[29–33] suggesting a systematic investigation to unveil the effect of oxygen deficiency and related factors on HER catalysis.

[a.] Department of Materials Science, Graduate School of Engineering, Osaka Prefecture University, 1-2 Gakuen-cho, Naka-ku, Sakai, Osaka 599-8570, Japan
*E-mail: yamada@mtr.osakafu-u.ac.jp (I.Y.)
[b.] Japan Synchrotron Radiation Research Institute (JASRI), 1-1-1 Kouto, Sayo-cho, Sayo-gun, Hyogo 679-5198, Japan
[c.] Department of Applied Chemistry, Faculty of Science and Engineering, Kindai University, 3-4-1 Kowakae, Higashi-Osaka, Osaka, 577-8502, Japan
[d.] Fuji Die Co., Ltd, 36-1 Hirasawa, Hadano, Kanagawa 257-0015, Japan
[e.] Institute of Industrial Science, The University of Tokyo, 4-6-1 Komaba, Meguro-ku, Tokyo 153-8505, Japan
† Footnotes relating to the title and/or authors should appear here.
Electronic Supplementary Information (ESI) available: [details of any supplementary information available should be included here]. See DOI: 10.1039/x0xx00000x

Herein, we demonstrate HER activity of $PBCO_{6-\delta}$ with a wide range of oxygen deficiency content ($0 \leq \delta \leq 0.85$). The highest activity was observed for $\delta = 0.2$, which was a top of the volcano-like plot. The origin of HER catalysis for $PBCO_{6-\delta}$ was investigated from the viewpoint of Co valence, electric conductivity, charge-transfer resistance, and oxygen deficiency content.

2. Experimental procedure

2.1. Sample Preparation

A pristine $PBCO_{5.8}$ sample was prepared by a conventional solid-state reaction. A stoichiometric amount of metal oxides and carbonate, Pr_6O_{11} (99.9%), $BaCO_3$ (99.9%), and Co_3O_4 (99.9%) were mixed at a mole ratio of 1:6:4. The mixture was heated in air at 1100 ºC for 24 h with intermediate grindings. A fully oxidized $PBCO_6$ was synthesized by a high-pressure treatment of $PBCO_{5.8}$. $PBCO_{5.8}$ was mixed with a $KClO_4$ oxidizing agent (99.5%) at a weight ratio of $PBCO_{5.8}$:$KClO_4$ = 10:1. The mixture was charged into a Pt capsule with 4 mm in diameter and 8 mm in height. The Pt capsule was put into an octahedral pressure-transmitting medium equipped with a graphite furnace. The sample included in the pressure-transmitting medium was compressed up to 8 GPa by using Walker-type high-pressure apparatus. The sample was heated up to 1000 ºC in 15 min and kept at the temperature for 30 min, followed by quench down to room temperature. The applied pressure was released after the heating. The sample was washed with deionized water for several times to remove remaining potassium chloride salts.

A slightly oxidized $PBCO_{5.9}$ was prepared by annealing $PBCO_6$ in the air at 150 ºC. A slightly reduced $PBCO_{5.7}$ was obtained by treating $PBCO_{5.8}$ at 8 GPa and 500 ºC for 30 min without mixing $KClO_4$. A moderately reduced $PBCO_{5.5}$ was obtained by quenching $PBCO_{5.8}$ from 1000 ºC in a nitrogen flow into liquid nitrogen. A strongly reduced $PBCO_{5.15}$ was also synthesized by a reductive annealing method from $PBCO_{5.8}$. $PBCO_{5.8}$ was pressed into a pellet and heated in a nitrogen flow at 1100 ºC for 12 h, followed by quench using liquid nitrogen. $ACoO_3$ (A = La, $La_{0.5}Ca_{0.5}$, and Ca) samples were synthesized from stoichiometric mixtures of constituent metal oxides in air (A = La) or at high-pressure (8 GPa; A = $La_{0.5}Ca_{0.5}$, and Ca) and high-temperature (500–1000 °C) conditions.[34] $Pr_{0.5}Ba_{0.25}Sr_{0.25}Co_{0.8}Fe_{0.2}O_{3-\delta}$ (PBSCF) was synthesized from stoichiometric mixture under ambient pressure and high temperature (1100 °C). Sr_2RuO_4 was synthesized by conventional solid-state reaction according to literature.[35] MoB powder (99.5%, 325 mesh) was purchased from Sigma-Aldrich. Commercial 30wt%-Pt/carbon composite (Pt/C) was purchased from Fuel Cell Earth.

2.2. Basic Characterization

Powder X-ray diffraction (XRD) measurement was conducted by using X-ray diffractometer with Cu Kα radiation (Ultima IV, Rigaku, Japan). Synchrotron X-ray powder diffraction (SXRD) data were collected at room temperature using a Debye-Scherrer camera installed at the BL02B2

beamline of SPring-8, Japan.[36] Crystal structure refinement was made using the Rietveld refinement program RIETAN-FP.[37] The specific surface area was estimated by the Brunauer-Emmett-Teller analysis (BET) of Kr gas adsorption data (BELSORP-max, MicrotracBEL, Japan). Oxygen content for $PBCO_{6-\delta}$ powder was determined by iodometric titration at least three times with a Hiranuma automatic titrator COM-1700A.[38] The X-ray absorption spectrum of Co K-edge was collected in transmission mode at the BL14B2 beamline of SPring-8. The electrical resistivity was measured by the standard dc four-probe method from 5 to 300 K using a Quantum Design Physical Property Measurements System. The sintered $PBCO_{6-\delta}$ pellet with a diameter of ~3 mm and a thickness of about 1–2 mm was prepared from the synthesized $PBCO_{6-\delta}$ powder by treating in the same conditions as the powder synthesis. Silver wires were connected to the $PBCO_{6-\delta}$ pellet with silver paste. Electrical conductivity was determined by the reciprocal of resistivity.

2.3. Electrochemical Characterization

Catalytic activities for HER were evaluated by using a rotating disk electrode system. According to the literature,[7,10,39] a 5 wt% proton-type Nafion suspension (Sigma-Aldrich), 0.1 M KOH aqueous solution (Nacalai Tesque Inc., Japan), and tetrahydrofuran (THF, Sigma-Aldrich) were mixed in a 2:1:97 volume ratio. The catalyst ink was prepared by mixing 5 mg of catalyst, 1 mg of acetylene black (Denka Co., Ltd., Japan), and 1 mL of the above THF solution. A 6.4 μL of catalyst ink was taken with stirring and drop cast onto the glassy carbon (GC) disk electrode (4 mm in diameter), yielding an approximate catalyst loading of 0.255 mg_{oxide} cm^{-2}. The GC disk electrode was pre-polished to a mirror finish with 0.05 μm α-Al_2O_3 slurries on a polishing cloth and rinsed with deionized water prior to electrode preparation. 16.67 mg of 30%-Pt/C (approximate Pt of 5 mg) was mixed with the 1mL of THF solution, and 6.4 μL of ink was cast onto the GC disk electrode. Electrochemical measurements were performed using a rotating-disk electrode rotator (RRDE-3A, BAS Inc., Japan) in combination with a bipotentiostat (Model-2325, BAS Inc., Japan). A Hg/HgO electrode (International Chemistry Co., Ltd., Japan) filled with a 1 M KOH aqueous solution (Nacalai Tesque, Inc., Japan) was used as the reference electrode. A graphite rod was used as the counter electrode.[40] All electrochemical measurements were conducted in 1 M KOH solution with H_2 saturation at room temperature. All potentials were calibrated to reversible hydrogen electrode (RHE) using the following equation: E_{RHE} (V vs. RHE) = $E_{Hg/HgO}$ (V vs. Hg/HgO) + 0.926. The disk potential was controlled to cathodic direction between –0.9 and –1.5 V versus Hg/HgO at a scan rate of 10 mV s^{-1}. The disk electrode was rotated at 1600 rpm. The data at the third scan were adopted because the data at the initial stage were unstable in the present experimental conditions. The *IR* compensation was conducted by using the resistance (R = 15 Ω) measured in advance. All current densities presented in this work were normalized with respect to the geometric area of GC electrode and with respect to the mass of the catalysts. The current densities of perovskites and MoB catalysts were also normalized with respect to the measured BET surface areas. The polarization curves were replotted as disk potential (vs. RHE)

versus the logarithm of |current density| to obtain Tafel plots. The linear portions of the Tafel plots were fitted to the Tafel equation (|disk potential| = $b$log|current density| + a) to obtain the Tafel slope (b). The chronopotentiometry (CP) measurements were at a constant cathodic current density of 10 mA cm$^{-2}_{disk}$ for 5000 seconds. Throughout these measurements, the RDE was rotated at 2400 rpm to remove H$_2$ gas bubbles generated at the catalyst surface. Electrochemical impedance spectra (EIS) were stimulated over the frequency range from 1 MHz to 0.1 Hz at –0.3 V vs. RHE. The EIS measurement was conducted after the three cathodic scans from –0.9 and –1.5 V versus Hg/HgO at a scan rate of 10 mV s^{-1}. All the EIS data were fitted by using the equivalent circuit in Figure S4, ESI.

2.4. Electronic Structure Calculations

Electronic structures of PrBaCo$_2$O$_5$, PrBaCo$_2$O$_{5.5}$, and PrBaCo$_2$O$_6$, were calculated within the framework of density functional theory (DFT). All the calculations were performed by the plane-wave-based projector augmented wave (PAW) method[41] with the Heyd-Scuseria-Ernzerhof (HSE)[42] hybrid functional as implemented in the VASP code.[43,44] The screening parameter in HSE functional was set to 0.2 Å^{-1}. The PAW dataset with radial cutoff 2.8, 2.8, 2.3, and 1.52 Bohr for Pr, Ba, Co, and O, respectively, where Pr-5s, 5p, 4f, 6s, 5d, Ba-5s, 5p, 6s, Co-3d, 4s, and O-2s, 2p electrons were explicitly treated as valence electrons. The plane-wave cutoff energy was set to 550 eV. For k-point sampling, the mesh $k_1 \times k_2 \times k_3$ was prepared in accordance with the Monkhorst-Pack scheme, where the mesh count in each direction was selected as the near-natural number of 40 per lattice parameter (1 Å^{-1}). The lattice constants and internal coordinates were optimized until the total energy difference, and residual forces converged to less than 10^{-5} and 10^{-2} eV Å^{-1}, respectively. The ferromagnetic structures were adopted for all the oxides.

3. Results and discussion

3.1. Synthesis and Basic Characterization

Figure 2a shows the XRD patterns of PBCO$_{6-\delta}$. All the samples were indexed with the double perovskite structures consisting of the layered ordering of Pr and Ba ions according to the literature.[29,30] Oxygen deficiency content (δ) determined by iodometric titration ranged between 0 and 0.85, as listed in Table S1 in ESI. According to the charge neutrality, the nominal Co valence was changed from +3.5 ($\delta = 0$) to +2.65 ($\delta = 0.85$).[38] The lattice volume per formula unit (V_{fu}) increased monotonically with increasing δ (Figure 2b). This can be interpreted as an increase in ionic radii of Co ions with the valence decrease. Apical oxygen atoms of CoO$_6$ octahedra at (Pr, O)-layers were preferentially removed when δ values increased whereas equatorial and apical oxygens at (Ba, O)-layers were retained, as reported previously.[32,33] We confirmed that the refined occupancy factors for apical oxygen sites at (Pr, O)-layers gradually decreased when δ values increased, as shown in Figure 2b (also see the Rietveld refinement result of SXRD data in Figure S1, Table S2 and S3, ESI). The Co K-edge absorption

edge in X-ray absorption near edge structure (XANES) monotonically shifted to a higher energy side with decreasing δ (Figure 3), confirming that the valence states of Co ions changed with the amount of oxygen deficiency. These results indicate that the oxygen deficiency content and Co valence for PBCO$_{6-\delta}$ samples mutually change in the isostructural framework.

Electrical resistivity systematically changed with δ. Figure 4a shows the temperature dependence of the dc electrical resistivity for PBCO$_{6-\delta}$. Almost temperature-independent behavior for $\delta = 0$ in the whole temperature range is attributed to the extrinsic effect of grain boundary resistance despite the intrinsic metallic property because of the polycrystalline sample.[30] In contrast, semiconductor-like behavior with strong temperature dependence was predominant when δ increased from 0.2 to 0.85. Figure 4b displays the fitting result of electrical conductivity (σ) with an Arrhenius-type function, ln$\sigma = -(E_a/k_B T) + C$, where E_a, k_B, T, and C are the activation energy, Boltzmann constant, temperature, and constant term, respectively. The activation energy increased with the δ value from ~6 meV ($\delta = 0$) to ~170 meV ($\delta = 0.85$), indicating the electronic state gradually changes from metallic to semiconducting with oxygen deficiency, which is consistent with the previous report.[30,45] The density of states (DOS) obtained by DFT calculation explains the change in electric conductivity. Figure 5 displays total/partial DOS in the vicinity of Fermi energy (set at $E = 0$ eV) for PBCO$_{6-\delta}$ ($\delta = 0$, 0.5, 1) (see DOS in the wide range in Figure S2, ESI). The total DOS at Fermi energy consisting of Co 3d and O 2p bands monotonically decreased when δ increased, reflecting electronic phase transformation from metallic to semiconducting.

3.2. Catalytic Activity

HER activity for PBCO$_{6-\delta}$ changed drastically in dependence upon δ. Figure 6a displays linear sweep voltammograms for PBCO$_{6-\delta}$. PBCO$_{5.8}$ exhibited the highest HER activity, whereas those with higher and lower δ had lower activities (also see Table 1). When the overpotentials (η_{onset}) were determined by HER onset potentials (E_{onset}) at –2 mA cm$^{-2}_{oxide}$: $\eta_{onset} = |E_{onset}|$ V, the η_{onset} once decreased from 0.27 V ($\delta = 0$) to 0.19 V ($\delta = 0.2$) and then increased to ~0.35 V ($\delta = 0.3$–0.85), forming volcano-like plot with δ (Figure 6c). The specific activities, which were defined as the current densities at –0.3 V vs. RHE, were changed simultaneously with η_{onset} (Figure 6d). This behavior reveals that the contribution of oxygen deficiency is not simple, but the complex effects associated with Co valence state are expected, resulting in the highest HER activity at a moderate value of $\delta = 0.2$.

The HER activity for PBCO$_{5.8}$ was comparable or superior to reported HER catalysts in alkaline solution, such as MoB, PBSCF,[46] and Sr$_2$RuO$_4$.[35] Figure 7a shows the linear sweep voltammograms for PBCO$_{5.8}$ and the reference catalysts (see their basic and electrochemical properties listed in Table 2). According to the literature,[23,47] overpotentials (η_{10}) determined by potentials reaching –10 mA cm$^{-2}_{disk}$ (E_{10} vs. RHE, $\eta_{10} = |E_{10}|$ V) were adopted. The bare GC disk electrode exhibited no activity, whereas the loading of catalysts substantially activated HER. PBCO$_{5.8}$ exhibited a much smaller overpotential ($\eta_{10} = 0.24$ V). This is superior to MoB ($\eta_{10} = 0.36$ V) and PBSCF (η_{10}

= 0.35 V),[46,48] and slightly inferior to Sr_2RuO_4 (η_{10} = 0.17 V) and Pt/C (η_{10} = 0.06 V). Figure 7b compares specific and mass activities at –0.3 V vs. RHE. $PBCO_{5.8}$ exhibited much higher activities than MoB and PBSCF, comparable to Sr_2RuO_4. Considering that $PBCO_{5.8}$ has a small specific surface area (0.47 m^2 g^{-1}) as well as other oxide catalysts (~0.5 m^2 g^{-1}), its high HER mass activity is not attributed to the surface area. The HER activity of $PBCO_{5.8}$ is lower than that of nanorod perovskite HER catalyst $SrCo_{0.7}Fe_{0.2}Nb_{0.1}O_3$ (η_{10} = 0.23 V) with large surface area (45 m^2 g^{-1}) at the present stage.[23] However, the HER activity of $PBCO_{5.8}$ could be further increased by processing. The durability of $PBCO_{5.8}$ was examined by chronopotentiometry measurement at a constant current density of –10 mA cm^{-2}_{disk} (Figure S3a, ESI). Cyclic voltammograms for $PBCO_{5.8}$ in continuous 100 cycles (Figure S3b, ESI) were collected to evaluate the stability. η_{onset} decreased significantly within the third cycle, and retained almost the steady state up to the 100th cycle. $PBCO_{5.8}$ exhibited a stable performance, excluding the possibility that the current is attributed to the sample reduction.

To unveil the origin of HER activity for $PBCO_{6-\delta}$, we examined HER activities for the simple perovskite oxide series without oxygen deficiency. Stoichiometric simple perovskite oxides (ACoO$_3$) consisting of aliovalent Co ions of Co^{3+} (A = La), $Co^{3.5+}$ (A = $La_{0.5}Ca_{0.5}$), and Co^{4+} (A = Ca) were obtained by using high-pressure conditions.[34] Figure 6b shows linear sweep voltammograms for $LaCoO_3$, $La_{0.5}Ca_{0.5}CoO_3$, and $CaCoO_3$ (also see Table 1). The η_{onset} monotonically shifted from 0.51 V (Co^{3+}) to 0.28 V (Co^{4+}) with increasing Co valence, leading to the highest HER activity for Co^{4+}. The monotonic increase (decrease) in specific activity (overpotential) with Co valence for ACoO$_3$ reveals that valence states predominantly affect the HER activity as well as OER activity, in which higher-valent Fe^{4+}/Co^{4+}-oxides exhibited higher OER/HER activities than lower-valent Fe^{3+}/Co^{3+}-oxides.[19] Note that this is the first observation that the HER activity simply increases with valence, proposing the transition metal valence as a useful descriptor for HER catalysis. Although it is apparently wondering that both oxidation (oxygen evolution) and reduction (hydrogen evolution) reactions are mutually enhanced for high valence oxides, the origin is basically interpreted by metal-oxygen covalency.[7] Sequential processes of Volmer and Heyrovsky/Tafel steps are proposed for HER on transition metal oxides.[23] In these steps, charge transfer between metal ions and the oxygen atom of adsorbate is expected to be enhanced by strong metal-oxygen covalency for HER as well as OER.[7] The detailed analysis of charge-transfer resistance supports this picture, as discussed later.

Figure 6c compares overall HER activities between ACoO$_3$ and $PBCO_{6-\delta}$. The overpotential in ACoO$_3$ monotonically decreases with Co valence from +3 to +4. In contrast, $PBCO_{6-\delta}$ forms a volcano-like plot with the top at δ = 0.2. A comparison between isoelectronic $Co^{3.5+}$ oxides without oxygen deficiency, $PBCO_6$ (η_{onset} = 0.27 V) and $La_{0.5}Ca_{0.5}CoO_3$ (η_{onset} = 0.43 V), evidences that the double-perovskite structure with the layered ordering of A-site ions is intrinsically superior to simple perovskite with randomly mixed A-site ions. This is probably because the periodic charge distribution derived from the atomic

ordering of Pr^{3+} and Ba^{2+} ions serves to activate the surface states more effectively than the random distribution of La^{3+} and Ca^{2+} ions, although the detailed mechanism is not clear at the present stage. Further interestingly, the baseline for $PBCO_{6-\delta}$ was closely overlapped by that for ACoO$_3$ with –0.17 V offset (Figure 6c), demonstrating that the valence effect on overpotential is also predominant for the double perovskite oxides. In addition to the Co valence dependence, the volcano-type plot was derived from the activation by oxygen deficiency for the double perovskite. Figure 6d compares specific activities between ACoO$_3$ and $PBCO_{6-\delta}$. Valence dependence was also predominant for ACoO$_3$ and the baseline of $PBCO_{6-\delta}$, being overlapped by the twelvefold activity of ACoO$_3$ as well as overpotentials.

Figure 8 shows Tafel plots for $PBCO_{6-\delta}$, obtaining Tafel slopes by linear fitting with Tafel equation.[49] A drastic change in Tafel slope from ~120 mV decade^{-1} (δ = 0) to 60–80 mV decade^{-1} (δ = 0.1–0.85) implies that oxygen deficiency sites facilitate the Volmer step with H_2O adsorption. This result is well consistent with the value of ~120 mV decade^{-1} for δ = 0 without oxygen deficiency, indicating that the rate-determining step is Volmer step.[49]

The charge-transfer resistance analysis supports the covalency-activated HER. Figure 9a displays Nyquist plots for ACoO$_3$ obtained from the EIS measurements at –0.3 V vs. RHE. All spectra consist of two (distorted) semicircles. Smaller semicircles with R ~ 25 Ω, which were commonly observed in high-frequency ranges, correspond to uncompensated resistances.[2] Larger semicircles in low-frequency ranges were assigned to charge-transfer resistances, which was reported to be the order of several ten Ω for highly active metal-oxide HER catalysts.[22,23] The charge-transfer resistance estimated by fitting with the equivalent circuit (Figure S4, ESI) monotonically decreased in the order of Co valence from ~3000 Ω ($LaCo^{3+}O_3$) to ~600 Ω ($La_{0.5}Ca_{0.5}Co^{3.5+}O_3$) to ~60 Ω ($CaCo^{4+}O_3$), also following the order of HER overpotential and specific activity. This tendency evidences that the high HER activity of Co^{4+} ion is attributed to fast charge-transfer kinetics. In contrast, much larger charge-transfer resistances for $LaCoO_3$ and $La_{0.5}Ca_{0.5}CoO_3$ were derived from slow charge-transfer related to the rate-determining step. $PBCO_{6-\delta}$ also demonstrated a strong dependence of charge-transfer resistance on Co valence (Figure 9b). $PBCO_{5.15}$ exhibited the most massive semicircle of ~300 Ω, whereas smaller circles of ~60 Ω were observed for $PBCO_{5.8}$ and $PBCO_{5.5}$, eventually the smallest for $PBCO_6$. This indicates that the charge-transfer kinetics is not dependent on the oxygen deficiency but is predominated by the Co valence. The above comparison reasonably separates the roles of Co valence and oxygen deficiency.

The HER activities of $Co^{3.5+}$-containing oxides, $La_{0.5}Ca_{0.5}CoO_3$ and $PBCO_6$, are compared in Figure 10a. The HER activity for $PBCO_6$ is higher than that for $La_{0.5}Ca_{0.5}CoO_3$, although both consist of the isovalent Co ions and contain no oxygen deficiency. Almost the same Tafel slopes of ~120 mV decade^{-1} indicates that the Volmer step is the rate-determining step for both (Figure 10b). The origin of the difference in HER activity is attributed to the charge-transfer resistance. Figure 10c illustrates the Nyquist plots, in which $PBCO_6$ exhibits much

smaller charge-transfer resistance compared with $La_{0.5}Ca_{0.5}CoO_3$. This observation reveals that a fast charge-transfer process is achieved in $PBCO_6$. Hence, the layered atomic ordering of *A*-site ions improves the kinetics of the charge-transfer process in HER probably because the periodic ordering of charge distribution is related to the fast charge transfer between active site and adsorbate.

The above results propose the following factors to activate HER. Firstly, a high valence state for transition metal increases charge-transfer kinetics because of metal-oxygen covalency, as well as OER. This factor is beneficial to Volmer and Heyrovsky steps, which involve charge-transfer in alkaline HER. Secondly, oxygen deficiency behaves as a water-adsorption/dissociation site, which is supported by smaller Tafel slopes for oxygen-deficient compounds. This is consistent with previous reports that the presence of oxygen deficiency on the surface of transition metal oxides significantly enhances the water dissociation.[21,50] It was also demonstrated that oxygen deficiency does not affect the charge-transfer kinetics. This factor promotes Volmer step associated with the water-adsorption/dissociation. Thirdly, *A*-site cation ordering improves the HER catalysis probably because of regular charge distribution. This factor may improve Volmer and Heyrovsky steps as well as high valence state. Finally, regardless of ordering/disordering of oxygen deficiency,[25] complementary contributions of Co valence and oxygen deficiency adjust the highest HER activity at moderate oxygen deficiency content ($\delta = 0.2$), which is comparable to the state-of-the-art HER catalysts. We examined the present results on HER overpotential versus *A*-site ionic negativity diagram recently proposed by Guan et al. (Figure 11).[26] In this diagram, we adopted the actual average values of *A*-site electronegativities: $\chi_{ave} = \Sigma f_i \chi_i$, where f_i and χ_i represent atomic fraction and electronegativity for *i*-th component at *A*-site, rather than the sum of electronegativities in the literature.[26] We observe two features in this diagram. Firstly, the overpotential linearly decreases with χ_{ave} for simple perovskite Co oxides at first glance. However, this behavior is derived from the valence change in Co ions, not predominantly attributed to the *A*-site ionic electronegativity. Secondly, the overpotential for $PBCO_{6-\delta}$ is distributed vertically in a range between 146 and 300 mV, which is much broader than those in the literature.[26] These features indicate that the application of *A*-site ionic electronegativity is limited to the selected compounds, and other factors, i.e., valence and oxygen deficiency, predominate HER.

4. Conclusions

In conclusion, we investigate the multiple factors to increase HER activity for perovskite-related Co oxides. Higher valence state contributes to fast charge-transfer via strong covalency between the transition metal and adsorption intermediates. Oxygen deficiency serves as the water-adsorption/dissociation site, which is revealed by the Tafel slope analysis. Furthermore, the *A*-site cation ordering solely increases HER activity by improving charge-transfer kinetics. The above factors can be arbitrarily combined, and an additional increase in HER activity is expected by optimizing these factors. We are now

investigating further improvement in HER for other *A*/*B*-site ordered perovskite oxides.

Conflicts of interest

There are no conflicts to declare.

Acknowledgements

Notes and references

1　A. R. Zeradjanin, J. P. Grote, G. Polymeros and K. J. J. Mayrhofer, A Critical Review on Hydrogen Evolution Electrocatalysis: Re-exploring the Volcano-relationship. *Electroanalysis*, 2016, **28**, 2256–2269.

2　W. T. Hong, M. Risch, K. A. Stoerzinger, A. Grimaud, J. Suntivich and Y. Shao-Horn, Toward the rational design of non-precious transition metal oxides for oxygen electrocatalysis. *Energy Environ. Sci.*, 2015, **8**, 1404–1427.

3　E. Fabbri and T. J. Schmidt, Oxygen Evolution Reaction - The Enigma in Water Electrolysis. *ACS Catal.*, 2018, **8**, 9765–9774.

4　P. Wang, M. Yan, J. Meng, G. Jiang, L. Qu, X. Pan, J. Z. Liu and L. Mai, Oxygen evolution reaction dynamics monitored by an individual nanosheet-based electronic circuit. *Nat. Commun.*, 2017, **8**, 645.

5　J. O. M. Bockris, T. Otagawa, J. E. Soc, J. O. M. Bockris and T. Otagawa, The Electrocatalysis of Oxygen Evolution on Perovskites. *J. Electrochem. Soc.*, 1984, **131**, 290–302.

6　J. O. M. Bockris and T. Otagawa, Mechanism of oxygen evolution on perovskites. *J. Phys. Chem.*, 1983, **87**, 2960–2971.

7　J. Suntivich, K. J. May, H. A. Gasteiger, J. B. Goodenough and Y. Shao-Horn, A perovskite oxide optimized for oxygen evolution catalysis from molecular orbital principles. *Science*, 2011, **334**, 1383–1385.

8　A. Grimaud, K. J. May, C. E. Carlton, Y. L. Lee, M. Risch, W. T. Hong, J. Zhou and Y. Shao-Horn, Double perovskites as a family of highly active catalysts for oxygen evolution in alkaline solution. *Nat. Commun.*, 2013, **4**, 2439.

9　Y. Zhu, W. Zhou, Z. G. Chen, Y. Chen, C. Su, M. O. Tadé and Z. Shao, $SrNb_{0.1}Co_{0.7}Fe_{0.2}O_{3-\delta}$ perovskite as a next-generation electrocatalyst for oxygen evolution in alkaline solution. *Angew. Chemie - Int. Ed.*, 2015, **54**, 3897–3901.

10　S. Yagi, I. Yamada, H. Tsukasaki, A. Seno, M. Murakami, H. Fujii, H. Chen, N. Umezawa, H. Abe, N. Nishiyama and

S. Mori, Covalency-reinforced oxygen evolution reaction catalyst. *Nat. Commun.*, 2015, **6**, 8249.

11 I. Yamada, H. Fujii, A. Takamatsu, H. Ikeno and K. Wada, Bifunctional Oxygen Reaction Catalysis of Quadruple Manganese Perovskites. *Adv. Mater.*, 2017, **29**, 1603004.

12 I. Yamada, Novel catalytic properties of quadruple perovskites. *Sci. Technol. Adv. Mater.*, 2017, **18**, 541–548.

13 Y. Chen, H. Li, J. Wang, Y. Du, S. Xi, Y. Sun, M. Sherburne, J. W. Ager, A. C. Fisher and Z. J. Xu, Exceptionally active iridium evolved from a pseudo-cubic perovskite for oxygen evolution in acid. *Nat. Commun.*, 2019, **10**, 572.

14 X. Li, H. Wang, Z. Cui, Y. Li, S. Xin, J. Zhou, Y. Long, C. Jin and J. B. Goodenough, Exceptional oxygen evolution reactivities on $CaCoO_3$ and $SrCoO_3$. *Sci. Adv.*, 2019, **5**, eaav6262.

15 Y. Zhu, H. A. Tahini, Z. Hu, Z. G. Chen, W. Zhou, A. C. Komarek, Q. Lin, H. J. Lin, C. Te Chen, Y. Zhong, M. T. Fernández-Díaz, S. C. Smith, H. Wang, M. Liu and Z. Shao, Boosting Oxygen Evolution Reaction by Creating Both Metal Ion and Lattice-Oxygen Active Sites in a Complex Oxide. *Adv. Mater.*, 2020, **32**, 1905025.

16 W. T. Hong, K. A. Stoerzinger, Y.-L. L. Lee, L. Giordano, A. Grimaud, A. M. Johnson, J. Hwang, E. J. Crumlin, W. Yang and Y. Shao-Horn, Charge-transfer-energy-dependent oxygen evolution reaction mechanisms for perovskite oxides. *Energy Environ. Sci.*, 2017, **10**, 2190–2200.

17 H. Li, Y. Chen, S. Xi, J. Wang, S. Sun, Y. Sun, Y. Du and Z. J. Xu, Degree of Geometric Tilting Determines the Activity of FeO_6 Octahedra for Water Oxidation. *Chem. Mater.*, 2018, **30**, 4313–4320.

18 I. Yamada, A. Takamatsu, K. Asai, H. Ohzuku, T. Shirakawa, T. Uchimura, S. Kawaguchi, H. Tsukasaki, S. Mori, K. Wada, H. Ikeno and S. Yagi, Synergistically Enhanced Oxygen Evolution Reaction Catalysis for Multielement Transition-Metal Oxides. *ACS Appl. Energy Mater.*, 2018, **1**, 3711–3721.

19 I. Yamada, A. Takamatsu, K. Asai, T. Shirakawa, H. Ohzuku, A. Seno, T. Uchimura, H. Fujii, S. Kawaguchi, K. Wada, H. Ikeno and S. Yagi, Systematic Study of Descriptors for Oxygen Evolution Reaction Catalysis in Perovskite Oxides. *J. Phys. Chem. C*, 2018, **122**, 27885–27892.

20 R. Subbaraman, D. Tripkovic, D. Strmcnik, K. C. Chang, M. Uchimura, a P. Paulikas, V. Stamenkovic and N. M. Markovic, Enhancing Hydrogen Evolution Activity in Water Splitting by Tailoring Li^+-Ni(OH) -Pt Interfaces. *Science*, 2011, **334**, 1256–1260.

21 T. Ling, D. Y. Yan, H. Wang, Y. Jiao, Z. Hu, Y. Zheng, L. Zheng, J. Mao, H. Liu, X. W. Du, M. Jaroniec and S. Z. Qiao, Activating cobalt (II) oxide nanorods for efficient electrocatalysis by strain engineering. *Nat. Commun.*, 2017, **8**, 1509.

22 J. Wang, Y. Gao, D. Chen, J. Liu, Z. Zhang, Z. Shao and F. Ciucci, Water Splitting with an Enhanced Bifunctional Double Perovskite. *ACS Catal.*, 2018, **8**, 364–371.

23 Y. Zhu, W. Zhou, Y. Zhong, Y. Bu, X. Chen, Q. Zhong, M. Liu and Z. Shao, A Perovskite Nanorod as Bifunctional Electrocatalyst for Overall Water Splitting. *Adv. Energy Mater.*, 2017, **7**, 1602122.

24 X. Xu, Y. Pan, W. Zhou, Y. Chen, Z. Zhang and Z. Shao, Toward Enhanced Oxygen Evolution on Perovskite Oxides Synthesized from Different Approaches: A Case Study of $Ba_{0.5}Sr_{0.5}Co_{0.8}Fe_{0.2}O_{3-\delta}$. *Electrochim. Acta*, 2016, **219**, 553–559.

25 D. Guan, J. Zhou, Z. Hu, W. Zhou, X. Xu, Y. Zhong, B. Liu, Y. Chen, M. Xu, H. J. Lin, C. Te Chen, J. Q. Wang and Z. Shao, Searching General Sufficient-and-Necessary Conditions for Ultrafast Hydrogen-Evolving Electrocatalysis. *Adv. Funct. Mater.*, 2019, **29**, 1900704.

26 D. Guan, J. Zhou, Y.-C. Huang, C.-L. Dong, J.-Q. Wang, W. Zhou and Z. Shao, Screening highly active perovskites for hydrogen-evolving reaction via unifying ionic electronegativity descriptor. *Nat. Commun.*, 2019, **10**, 3755.

27 Q. Sun, Z. Dai, Z. Zhang, Z. Chen, H. Lin, Y. Gao and D. Chen, Double perovskite $PrBaCo_2O_{5.5}$: An efficient and stable electrocatalyst for hydrogen evolution reaction. *J. Power Sources*, 2019, **427**, 194–200.

28 K. Momma and F. Izumi, VESTA 3 for three-dimensional visualization of crystal, volumetric and morphology data. *J. Appl. Crystallogr.*, 2011, **44**, 1272–1276.

29 D. S. Tsvetkov, I. L. Ivanov, D. A. Malyshkin and A. Y. Zuev, Oxygen content, cobalt oxide exsolution and defect structure of the double perovskite $PrBaCo_2O_{6-\delta}$. *J. Mater. Chem. A*, 2016, **4**, 1962–1969.

30 M. Motin Seikh, V. Pralong, O. I. Lebedev, V. Caignaert and B. Raveau, The ordered double perovskite $PrBaCo_2O_6$: Synthesis, structure, and magnetism. *J. Appl. Phys.*, 2013, **114**, 013902.

31 C. Frontera, J. L. García-Muñoz, A. E. Carrillo and A. Caneiro, Spin state and magnetic interactions of Co^{3+} in $PrBaCo_2O_{5.50}$. *J. Magn. Magn. Mater.*, 2007, **316**, e731–e733.

32 S. Streule, A. Podlesnyak, D. Sheptyakov, E. Pomjakushina, M. Stingaciu, K. Conder, M. Medarde, M. V. Patrakeev, I. A. Leonidov, V. L. Kozhevnikov and J. Mesot, High-temperature order-disorder transition and polaronic conductivity in $PrBaCo_2O_{5.48}$. *Phys. Rev. B - Condens. Matter Mater. Phys.*, 2006, **73**, 094203.

33 S. Streule, A. Podlesnyak, J. Mesot, M. Medarde, K. Conder, E. Pomjakushina, E. Mitberg and V. Kozhevnikov, Effect of oxygen ordering on the structural and magnetic properties of the layered perovskites $PrBaCo_2O_{5+\delta}$. *J. Phys. Condens. Matter*, 2005, **17**, 3317–3324.

34 T. Osaka, H. Takahashi, H. Sagayama, Y. Yamasaki and S. Ishiwata, High-pressure synthesis of an unusual antiferromagnetic metal $CaCoO_3$ with $GdFeO_3$-type perovskite structure. *Phys. Rev. B*, 2017, **95**, 224440.

35 Y. Zhu, H. A. Tahini, Z. Hu, J. Dai, Y. Chen, H. Sun, W. Zhou, M. Liu, S. C. Smith, H. Wang and Z. Shao, Unusual synergistic effect in layered Ruddlesden−Popper oxide enables ultrafast hydrogen evolution. *Nat. Commun.*, 2019, **10**, 149.
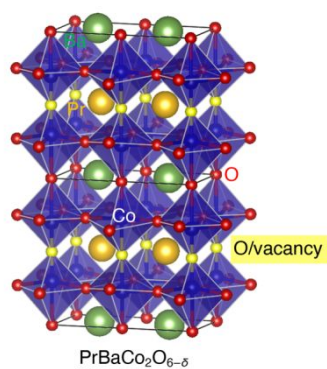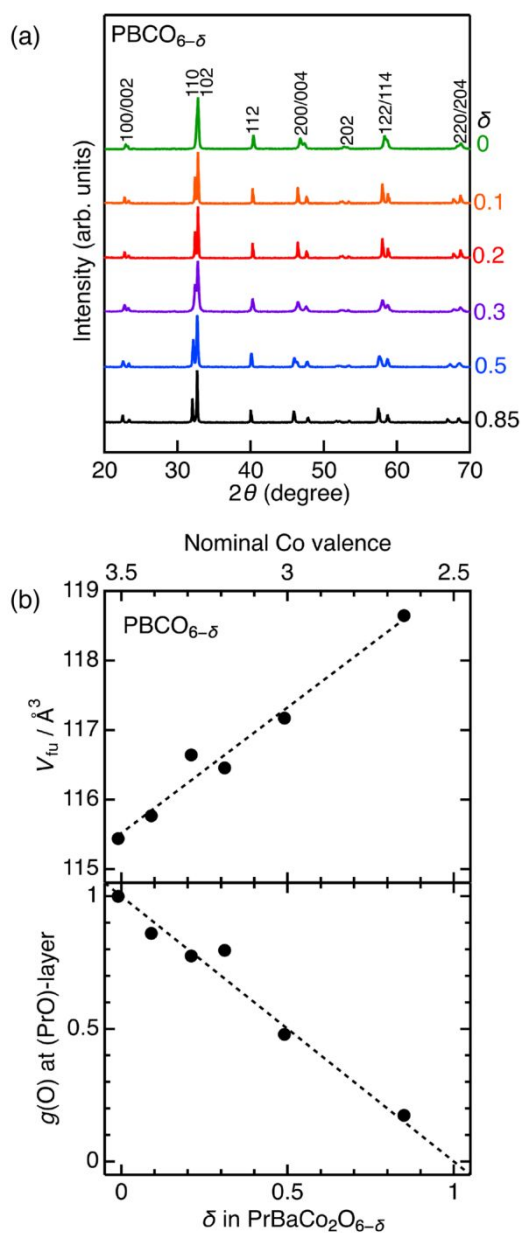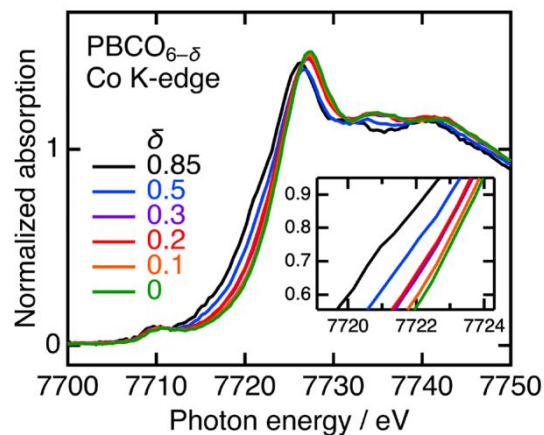
36   S. Kawaguchi, M. Takemoto, K. Osaka, E. Nishibori, C. Moriyoshi, Y. Kubota, Y. Kuroiwa and K. Sugimoto, High-throughput powder diffraction measurement system consisting of multiple MYTHEN detectors at beamline BL02B2 of SPring-8. *Rev. Sci. Instrum.*, 2017, **88**, 85111.

37   F. Izumi and K. Momma, Three-Dimensional Visualization in Powder Diffraction. *Solid State Phenom.*, 2007, **130**, 15–20.

38   M. Karppinen, M. Matvejeff, K. Salomäki and H. Yamauchi, Oxygen content analysis of functional perovskite-derived cobalt oxides. *J. Mater. Chem.*, 2002, **12**, 1761–1764.

39   I. Yamada, H. Fujii, A. Takamatsu, H. Ikeno, K. Wada, H. Tsukasaki, S. Kawaguchi, S. Mori and S. Yagi, Bifunctional Oxygen Reaction Catalysis of Quadruple Manganese Perovskites. *Adv. Mater.*, 2017, **29**, 1603004.

40   R. Chen, C. Yang, W. Cai, H. Y. Wang, J. Miao, L. Zhang, S. Chen and B. Liu, Use of Platinum as the Counter Electrode to Study the Activity of Nonprecious Metal Catalysts for the Hydrogen Evolution Reaction. *ACS Energy Lett.*, 2017, **2**, 1070–1075.

41   P. E. Blochl, Projector Augmented-Wave Method. *Phys. Rev. B*, 1994, **50**, 17953–17979.

42   J. Heyd, G. E. Scuseria and M. Ernzerhof, Hybrid functionals based on a screened Coulomb potential. *J. Chem. Phys.*, 2003, **118**, 8207–8215.

43   G. Kresse and J. Furthmüller, Efficient iterative schemes for ab initio total-energy calculations using a plane-wave basis set. *Phys. Rev. B*, 1996, **54**, 11169–11186.

44   G. Kresse, Efficiency of ab-initio total energy calculations for metals and semiconductors using a plane-wave basis set. *Comput. Mater. Sci.*, 1996, **6**, 15–50.

45   X.-H. Lin, C.-H. Wang, X. Zhang, X.-P. Jing, Y. Zhang, C. Chen, H.-W. Wei and X.-M. Wang, Effect of oxygen content on transport and magnetic properties of $PrBaCo_2O_{5.50+\delta}$. *Mater. Res. Bull.*, 2015, **65**, 80–88.

46   X. Xu, Y. Chen, W. Zhou, Z. Zhu, C. Su, M. Liu and Z. Shao, A Perovskite Electrocatalyst for Efficient Hydrogen Evolution Reaction. *Adv. Mater.*, 2016, **28**, 6442–6448.

47   Y. Guo, Y. Tong, P. Chen, K. Xu, J. Zhao, Y. Lin, W. Chu, Z. Peng, C. Wu and Y. Xie, Engineering the Electronic State of a Perovskite Electrocatalyst for Synergistically Enhanced Oxygen Evolution Reaction. *Adv. Mater.*, 2015, **27**, 5989–5994.

48   H. Vrubel and X. Hu, Molybdenum boride and carbide catalyze hydrogen evolution in both acidic and basic solutions. *Angew. Chemie - Int. Ed.*, 2012, **51**, 12703–12706.

49   T. Shinagawa, A. T. Garcia-Esparza and K. Takanabe, Insight on Tafel slopes from a microkinetic analysis of aqueous electrocatalysis for energy conversion. *Sci. Rep.*, 2015, **5**, 13801.

50   J. Carrasco, D. Lõpez-Durán, Z. Liu, T. Duchoň, J. Evans, S. D. Senanayake, E. J. Crumlin, V. Matolín, J. A. Rodríguez and M. V. Ganduglia-Pirovano, In situ and theoretical studies for the dissociation of water on an active Ni/CeO_2 Catalyst: Importance of strong metal-support

interactions for the cleavage of O-H bonds. *Angew. Chemie - Int. Ed.*, 2015, **54**, 3917–3921.

51   K. Li and D. Xue, Estimation of electronegativity values of elements in different valence states. *J. Phys. Chem. A*, 2006, **110**, 11332–11337.

Table 1. Specific surface areas (A_s), HER onset overpotentials (η_{onset}) determined at onset current density of −2 mA cm$^{-2}_{oxide}$, overpotentials determined at −1 mA cm$^{-2}_{oxide}$ (η_1), specific activities (SA) at −0.3 V vs. RHE, Tafel slopes for PBCO$_{6-\delta}$ and references, and average A-site ionic electronegativity. The electronegativity values were calculated according to the reference.[51]

Compound	A_s (m^2 g^{-1})	η_{onset} (V)	η_1 (V)	SA (mA cm$^{-2}_{oxide}$)	Tafel slope (mV decade^{-1})	Average A-site ionic electronegativity
PBCO$_{5.15}$	1.01	0.34	0.30	1.02	87	1.17
PBCO$_{5.5}$	1.17	0.33	0.30	1.17	70	1.17
PBCO$_{5.7}$	1.71	0.35	0.29	1.13	79	1.17
PBCO$_{5.8}$	0.47	0.19	0.15	33.8	61	1.17
PBCO$_{5.9}$	1.54	0.26	0.24	5.20	64	1.17
PBCO$_6$	1.27	0.27	0.23	3.31	120	1.17
LaCoO$_3$	0.76	0.51	0.47	0.0900	116	1.23
La$_{0.5}$Ca$_{0.5}$CoO$_3$	2.4	0.43	0.38	0.241	119	1.16
CaCoO$_3$	1.3	0.28	0.26	3.49	75	1.09

Table 2. Specific surface areas (A_s), overpotentials determined at −10 mA cm$^{-2}_{disk}$ (η_{10}), and specific and mass activities (SA and MA) at −0.3 V vs. RHE for PrBaCo$_2$O$_{5.8}$, MoB, Pr$_{0.5}$Ba$_{0.25}$Sr$_{0.25}$Co$_{0.8}$Fe$_{0.2}$O$_{3-\delta}$ (PBSCF) and Sr$_2$RuO$_4$, and Pt/C.

Catalyst	A_s (m^2 g^{-1})	η_{10} (V)	SA (mA cm$^{-2}_{catalyst}$)	MA (A g^{-1})	Tafel slope (mV decade^{-1})
PBCO$_{5.8}$	0.47	0.24	33.8	157	61
MoB	0.11	0.36	13.1	14.4	95
PBSCF	0.49	0.35	3.29	16.2	64
Sr$_2$RuO$_4$	0.56	0.17	20.8	116	110
Pt/C	NA	0.06	NA	597	56

Figure 1. Schematic of crystal structure of $PBCO_{6-\delta}$.

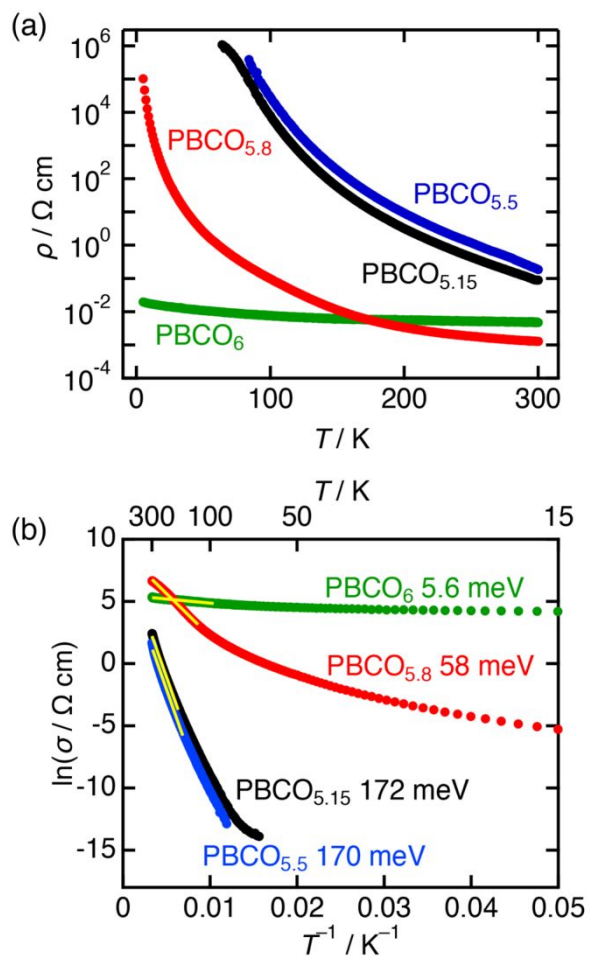Figure 3. XANES spectra at Co K-edge for $PBCO_{6-\delta}$. The inset shows enlarged spectra near edge.

Figure 2. (a) XRD patterns for $PBCO_{6-\delta}$. (b) δ dependence of cell volume and refined occupancy factor at O site in (Pr,O)-layer for $PBCO_{6-\delta}$.

Figure 4. (a) Temperature dependence of resistivity for $PBCO_{6-\delta}$. (b) Logarithm of electrical conductivity ($\ln\sigma$) versus inverse temperature (T^{-1}) for $PBCO_{6-\delta}$.
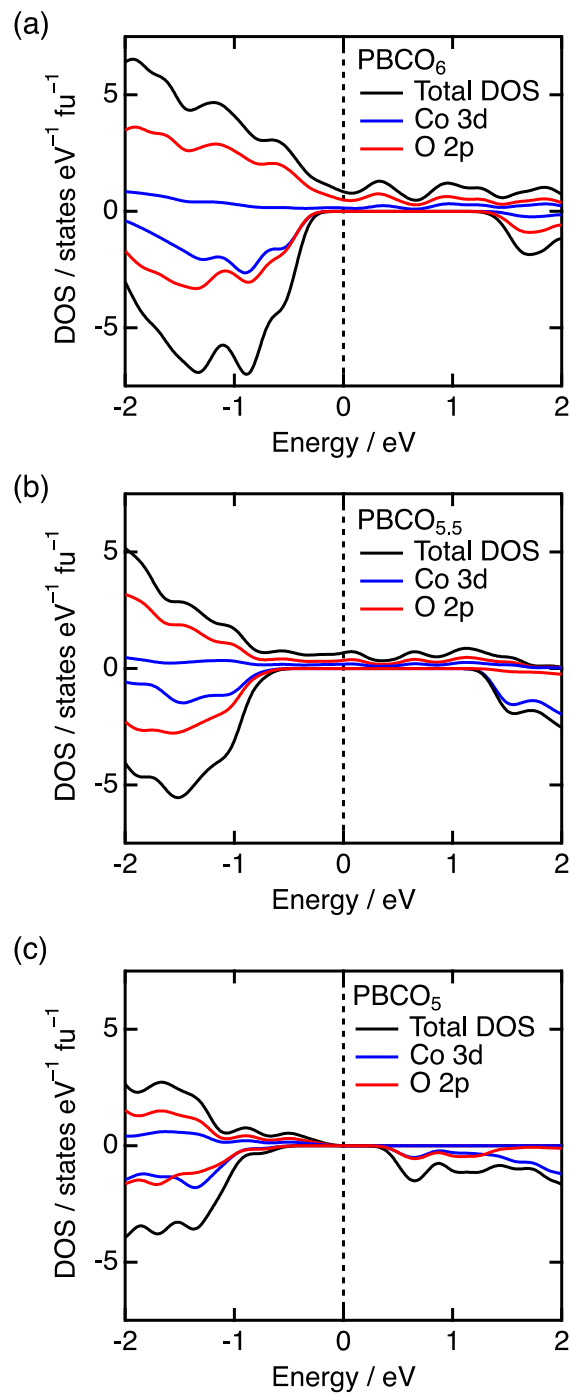
Figure 5. Total and partial density of states (DOS) for (a) $PBCO_6$, (b) $PBCO_{5.5}$, and (c) $PBCO_5$ obtained from DFT calculation.
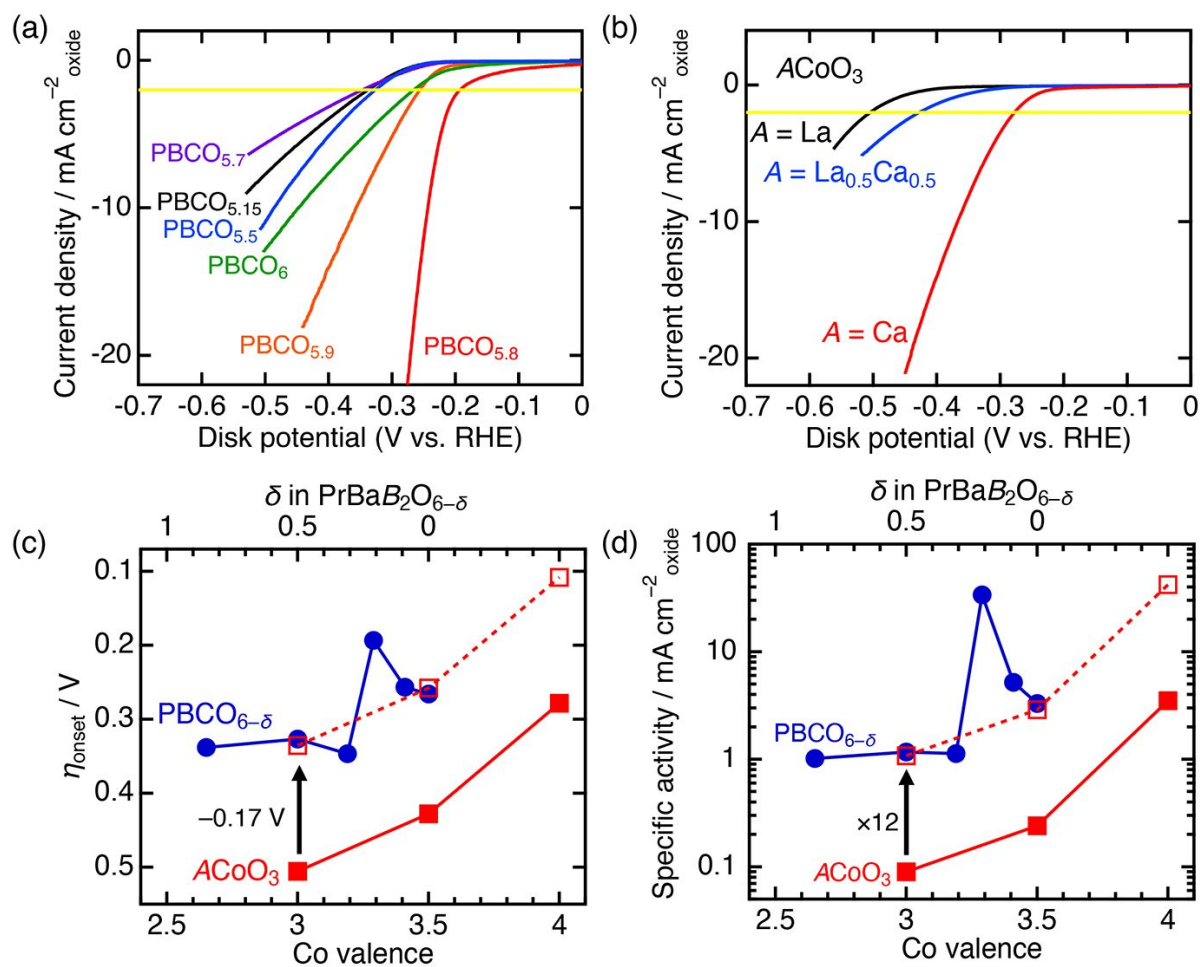
Figure 6. Linear sweep voltammograms for (a) PBCO$_{6-\delta}$ and (b) ACoO$_3$ (A = La, La$_{0.5}$Ca$_{0.5}$, Ca) measured in 1 M KOH aqueous solution at 10 mV s^{-1}. (c) HER overpotential and (d) specific activity as a function of Co valence and δ for ACoO$_3$ (red) and PBCO$_{6-\delta}$ (blue).
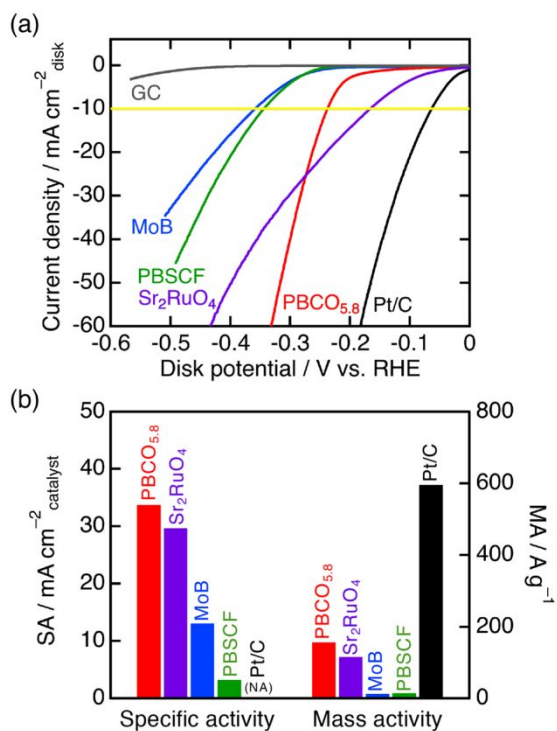
Figure 7. (a) Linear sweep voltammograms for PBCO$_{5.8}$ and reference catalysts measured in 1 M KOH aqueous solution at 10 mV s^{-1}. (b) Specific activity (SA) and mass activity (MA) for PBCO$_{5.8}$ and references at –0.3 V vs. RHE.
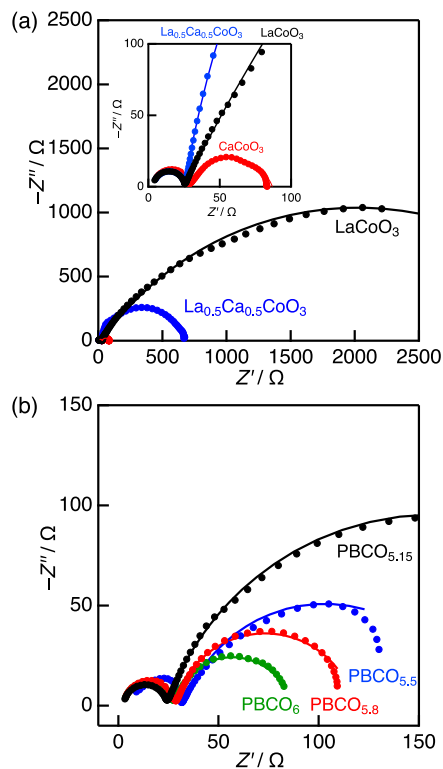

Figure 9. Nyquist plots measured in 1 M KOH aqueous solution stimulated over the frequency range from 1 MHz to 0.1 Hz at –0.3 V vs. RHE for (a) ACoO$_3$ and (b) PBCO$_{6-\delta}$.

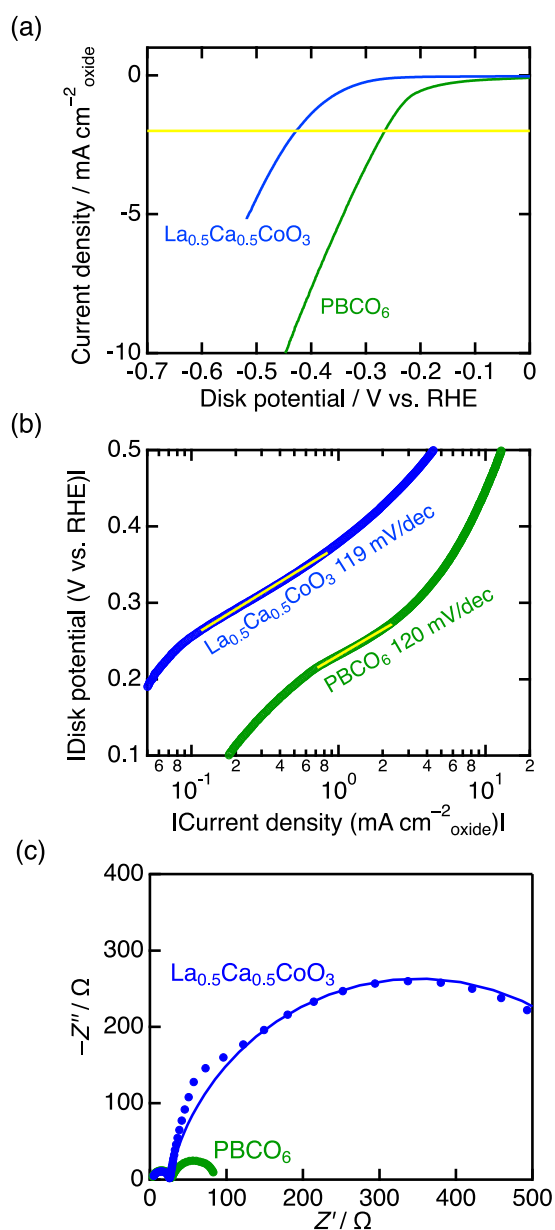Figure 8. Tafel plots for PBCO$_{6-\delta}$.

(a)

(b)

(c)

Figure 10. (a) Linear sweep voltammograms measured in 1 M KOH aqueous solution at 10 mV s⁻¹, (b) Tafel plots, and (c) EIS Nyquist plots measured in 1 M KOH aqueous solution stimulated over the frequency range from 1 MHz to 0.1 Hz at –0.3 V vs. RHE for $La_{0.5}Ca_{0.5}CoO_3$ and $PBCO_6$.
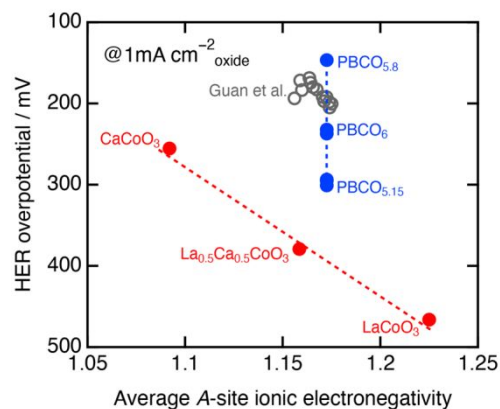

Figure 11. HER overpotential versus Average A-site ionic electronegativity for simple (red) and double (blue) perovskite oxides. The overpotentials (η_1) were determined by the onset potentials at the current density of 1 mA cm⁻²$_{oxide}$. The data reported by Guan et al. (gray open circles) were taken from the reference.[26]